RESEARCH ARTICLE

Open Source Sensor Interface for Soft Detectors in Surgical Simulators

THOMAS THURNER[1,2], **ROLAND PRUCKNER**[2,3],
MARTIN KALTENBRUNNER[2,3], **(Member, IEEE),**
AND ANDREAS SCHREMPF[1]

[1]Research Group for Surgical Simulators Linz (ReSSL), Upper Austria University of Applied Sciences, 4020 Linz, Austria
[2]Division of Soft Matter Physics, Institute for Experimental Physics, Johannes Kepler University, 4040 Linz, Austria
[3]Soft Materials Laboratory, Linz Institute of Technology, Johannes Kepler University, 4040 Linz, Austria

Corresponding author: Thomas Thurner (thomas.thurner@fh-linz.at)

ABSTRACT Surgical simulation is an emerging area of research and development, making new developments of especially hybrid simulators highly relevant. In this context, soft sensors enable low-cost position or force detection in haptically realistic synthetic tissue imitations to link the physical and virtual components of a patient phantom. To accelerate and facilitate the development of such simulators, an open-source sensor interface module optimized for use with soft carbon black silicone composite based sensors is presented. The module can measure complex voltages and impedances between multiple measurement channels at various frequencies. This enables up to three-dimensional tool tracking of conductive surgical instruments in patient phantoms as well as force or deformation detection at relevant structures. Several application scenarios are presented. Disruptive influences on the sensors are minimized by evaluating the signals based on discrete Fourier transform. Higher frequency signal coupling avoids contacting problems with soft sensors, which are often highly piezoresistive. Compensation functions or favorable sensor structures can largely avoid the influence of parasitic capacitances, which are particularly prevalent in low-cost electronics. The universally applicable module provides all the necessary electronics, including firmware and software interface for the subsequent processing computer. The handy module offers 17 measuring channels as well as digital inputs and outputs and is operated via USB. In addition to the evaluability of various sensor types relevant for surgical simulation, electroimpedance tomography is also supported, as demonstrated by the examples.

INDEX TERMS Soft sensors, surgical simulator, sensor interface, low-cost, open source, multichannel.

I. INTRODUCTION

Surgical simulation is an emerging research field that has already proven its importance [1], [2]. Simulators are designed to accelerate the acquisition of essential motor skills and knowledge about surgeries while providing a safe environment for surgeons in training and increased patient safety. The evolution of simulators [2] went through several stages, from initial cadaver training over, among other things, passive artificial replicas to purely virtual simulators including virtual, augmented or mixed reality [3]. However, haptic feedback, which is essential [4], is completely absent in purely virtual simulators. Therefore, the class of hybrid simulators extends virtual simulators by including haptic feedback [5], [6], which is achieved through a sophisticated linking of physical and virtual simulator components. This ensures comprehensive learning success, and sometimes even original surgical instruments can be used [7].

For the synchronization of physical patient phantoms and virtual software components, and to provide the possibility of qualitative and quantitative feedback on the success/failure of a trained surgery, sensors are required. To avoid expensive

---

The associate editor coordinating the review of this manuscript and approving it for publication was Riccardo Carotenuto.

electromagnetic [5] and optical [8] tracking systems in surgical simulators, soft sensors inside physical patient phantoms are cost-efficient and sophisticated alternatives. They allow relative position detection in soft and deformable synthetic tissue imitations [7] to evaluate the manipulation of flexible target areas. Haptics are not distorted by such soft sensors and real surgical instruments can be used to optimally train motor skills related to instrument handling.

The objective of most simulated surgical interventions is to reach, expose, or manipulate specific target areas while avoiding damage to surrounding tissue. Because of the similarity of these procedures, it is expedient to have a unified system of sensor-to-computer interfaces.

To facilitate the use of soft sensors in surgical simulators and minimize the development time and costs for such indispensable devices, an interface between a computer and sensors is presented, provided with circuits, CAD data, software, and firmware. The system was optimized for use with soft carbon-black-silicone composites [9], [10] and was designed to ensure the greatest possible flexibility in terms of application. This is intended to reduce the development effort by eliminating the need for electronic design, while also simplifying the application through object classes and plug-and-play character.

II. METHODES

A. USE CASES AND REQUIREMENTS

An interface between sensors and a computer should be tailored to the nature of its application to operate efficiently. Application scenarios can be roughly divided into two categories: applications with insertion tools, and tactile applications.

The first category, with insertion tools that should be electrically conductive, enables measurements directly via the tool as a measurement electrode. The capabilities of such sensors are schematically shown in Figures 1a – 1d. One-dimensional (1D) position detection of a needle inserted into a line-shaped sensor (Figure 1a) can be easily implemented as a voltage divider (e.g., position detection along blood vessels or nerves). An extension of the line-shaped sensor to a surface is also possible. By combining two such surfaces [11], position detection in independent directions can be realized (1.5D, Figure 1b). Further refinement is the realization of two-dimensional (2D) position detection within one layer (Figure 1c) [7], [12] based on resistivity measurements or electric field distributions. By combining multiple 2D sensor layers, resolution in the third spatial dimension (2.5D) can be achieved (Figure 1d). Of course, a cube-shaped sensor (extension of the concept from Figure 1c by the third dimension) would also be conceivable for true three-dimensional position detection (3D), assuming that only the tip of an inserted tool is conductive.

The second category refers to tactile sensors (Figures 1e – 1h) that can detect strain or deformation [13]. The simplest case corresponds to a strain gauge
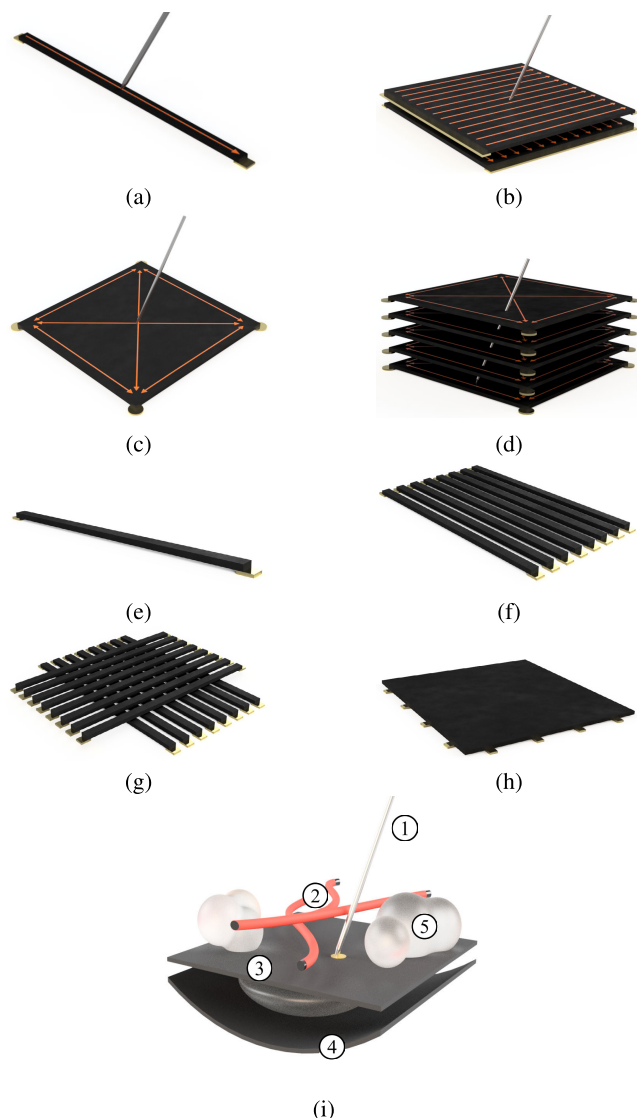
FIGURE 1. Possible application scenarios for soft sensor technology (grey needle, golden electrodes). (a) to (d) show applications for piercing with insertion tools: (a) 1D case using a linear sensor, (b) 1.5D case using two combined, planar extended 1D sensors, (c) 2D case with electrodes in the corners of the planar sensor, (d) 2.5D case using several 2D sensors arranged above each other. (e) to (h) show applications as tactile sensors for applied forces or deformations: (e) base element of deformation or force sensors, (f) repeated arrangement of base elements to obtain 1D resolution, (g) 1.5D case by orthogonal combination of two arrangements as in 1D, (h) 2D case by electrodes placed around a continuous sensor surface, continuous resolution of deformations can be achieved by electroimpedance tomography. (i) shows a combined application scenario: Insertion tool (1) in soft synthetic tissue, sensory blood vessels (red) as 1D sensor examples (2), position sensing surface as 2D sensor (3), depth detection layer (4) as a simple extension into the third dimension and, if necessary, haptic or optical adaptations (5) of the surrounding tissue.

(Figure 1e) [10]. However, such sensors can also be implemented as pressure cells. Several strain gauges arranged in a row result in a 1D resolution (Figure 1f). Again, a second dimension can be accessed by combining two 1D sensor arrangements (Figure 1g). Arrays of discrete sensors are also possible [14], [15], [16]. Using electro-impedance

tomography, continuous sensor layers can be used (Figure 1h) as 2D tactile sensors [17], [18], [19]. The resistivity distribution of the sensor mat can be determined by solving the inverse problem of field distributions by electrical excitation. Such sensors can be used among other things to detect undesirable mechanical stresses in sensitive tissues.

An exemplary demonstrator in Figure 1i illustrates a combination of different sensor types. This represents a realistic application scenario of soft sensor technology in haptically realistic synthetic soft tissue (surrounding material not shown). Similar to a biopsy, a needle should be inserted into a target region (shown in gold on the 2D sensor mat). Violations of larger blood vessels, and thus, contact with them, should be avoided. Feedback on the correctness of the achieved position can be provided via the 2D position detection of the sensor layer. This layer can also be used for the detection of excessive forces resulting in deformations, which would traumatize the tissue and should therefore be avoided as much as possible. An underlying sensor mat can provide depth information if the underlying tissue must not be reached, thus extending position detection by the third dimension. Curved surfaces can also be realized. Additionally, it is possible to supplement the surrounding fabric with haptic or optical features.

To enable the operation of such a demonstrator, an electronic system that can determine voltages, currents, and impedances on several channels is required. In addition, each channel should allow the injection of voltages or currents, as they are necessary for the formation of electric fields or excitation in electro impedance tomography (EIT) [20, pp. 1–30]. Other necessary requirements include mechanical and electrical robustness, insensitivity to interference, low cost, and simplicity of use.

According to Zou et al. [21], the performance of smart tactile sensor systems can be improved by enhancing sensor materials and fabrication technologies, as well as signal processing and algorithms. The proposed system covers the middle part of this process chain as a link between physical sensors and software algorithms (Figure 2).

The actual position of the proposed interface between a computer and sensors is shown in Figure 2.
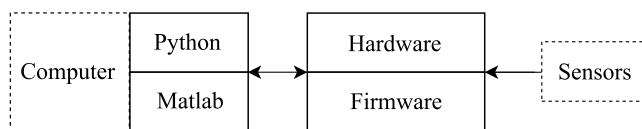
FIGURE 2. Overview of the sensory interface. The interface module interacts as bridge between a computer with third party software and sensors.

B. ELECTRONIC HARDWARE
The requirements for data acquisition of the soft sensors were met using a specially developed circuit. Low-cost basic circuits for EIT applications [17], [19] were used as a starting point, taking into account further accuracy-improving aspects of EIT [20, pp. 53–77]. Functionalities specifically for surgical simulators (as specified in Chapter II-A) were also integrated to allow the detection of conductive insertion tools. Because the contact points of electrodes to the soft sensor material (carbon-black-silicone composites) often exhibit considerable contact resistances [7] owing to impurities, boundary, or oxide layers, details of capacitive incoupling of signals were taken into account [22]. These and further subtleties regarding the improvement of the signal-to-noise ratio (SNR) [23] were considered in the circuit design.

In addition, general-purpose inputs/outputs (GPIO) have been added to make the application possibilities even more flexible (achieved through built-in MCP23017, Microchip Technology Inc., Chandler, Arizona, United States). Four status LEDs were added to indicate the measurement status, events or errors.

A block diagram of the developed circuit is shown in Figure 3.

This sensory interface circuit (SIC) is essentially an impedance sensing circuit based on the AD5933 (Analog Devices Inc., Norwood, Massachusetts, United States) integrated circuit (IC) for bio-impedance measurements. The blocks ''signal generator'' and ''ADC and signal processing'' shown in Figure 3 are features of AD5933. In general, the signal generator generates a sine wave signal with a selectable frequency between 1 kHz and 100 kHz. The analogue digital converter (ADC) of AD5933 has a resolution of 12 bits at a sampling rate of 1 MSPS. The acquired data is processed further on the IC by means of a discrete Fourier transformation (DFT), and only the frequency components matching the frequency of the signal generator are forwarded to a microcontroller (ATMEGA 32U4, Microchip Technology Inc., Chandler, Arizona, United States).

The microcontroller is part of a microcontroller-board called Pro Micro (DEV-12640, SparkFun Electronics, Niwot, Colorado, United States), which can be optionally pulled out of the designated slot. This allows the optional operation of SIC with other microcontrollers because all components are accessible via an externally accessible I^2C bus.

The signal generated from the AD5933 was adjusted to offset and amplitude by an amplifier. In general, all the amplifiers are of type AD8606 (Analog Devices Inc., Norwood, Massachusetts, United States).

The integration of three multiplexers (MUX, 1–3) allows the operation of SIC with up to 16 measuring electrodes (ADG1606, Analog Devices Inc., Norwood, Massachusetts, United States).

In addition, it is possible to switch between two basic modes: impedance and voltage measurements. The latter enables the acquisition of electrical potentials based on insertable stimulation currents or voltages. This flexibility is intended to enable the broadest possible acquisition of accessible measured values. Switching can be performed via integrated analog switches S1–S4 (ADG1611, Analog Devices Inc., Norwood, Massachusetts, United States).
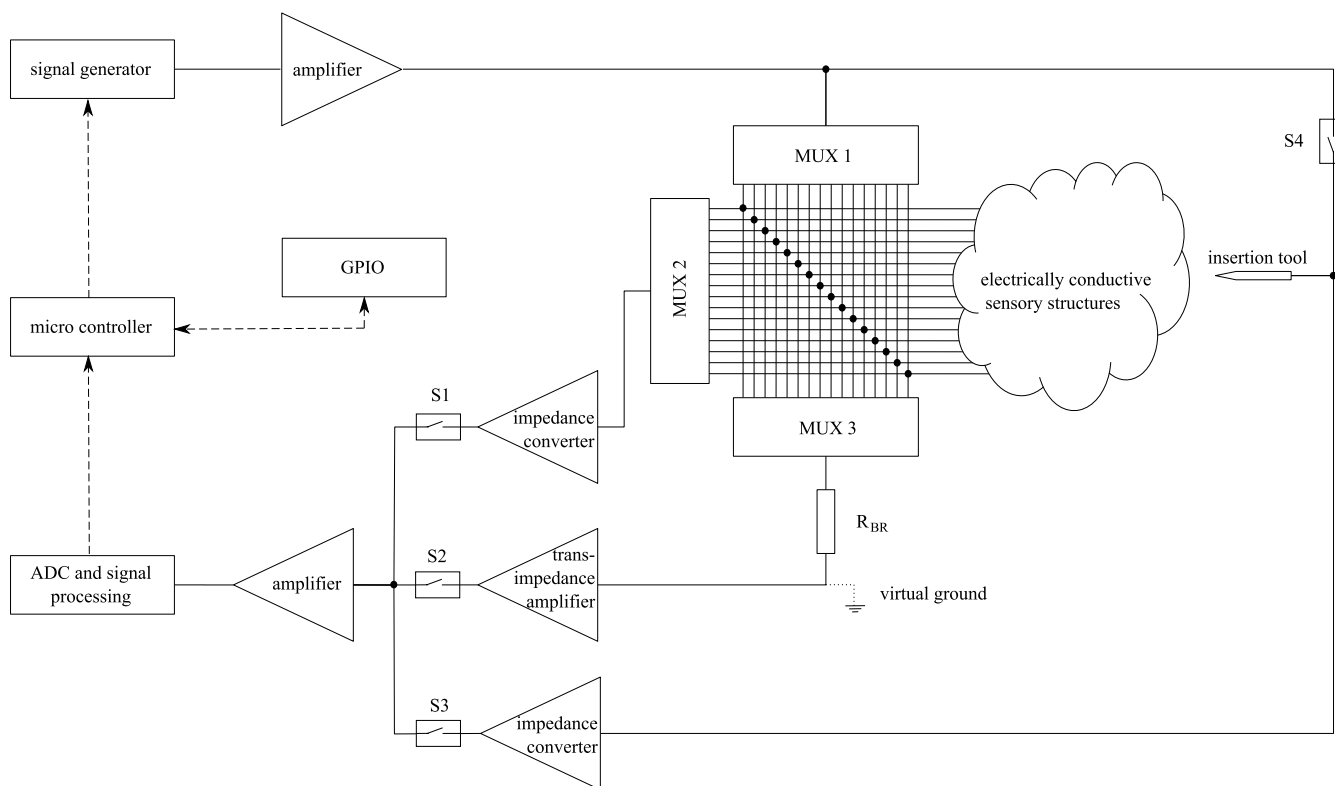
FIGURE 3. Block diagram of the Sensory interface circuit.

The forwarding of the amplified excitation signal to one of the 16 electrodes was realized via MUX 1. These electrodes can be fixed to any conductive sensors. Another built in MUX 3 receives the signal from any other electrode and allows it to be forwarded further via a basic resistor against the virtual ground. A transimpedance amplifier was placed to convert the corresponding electric current back into voltage. This voltage can be coupled into another amplifier (partly within AD5933) via analog switch S2, allowing the voltage to be adapted to the measurement range of AD5933 for optimal resolution. The latter voltage can now bDer Mickrokontroller sollte auch die Signalelektronik mit einem Computer verbinden.e evaluated because it contains information about the current flow through soft sensors. As the signal amplitude and electrical current are known, the impedance can be determined ($\underline{Z} = \frac{u_{\text{signal}}}{\underline{i}}$, with $\underline{Z}$ is the complex impedance, $\underline{u}_{\text{signal}}$ is the complex source signal voltage, and $\underline{i}$ is the complex current).

Alternatively, the amplified signal of the signal generator can also be routed via analog switch S4 into an insertion tool to flow through the conductive structures of the soft sensor system to one of the electrodes activated by MUX 3. Therefore, the insertion tool can be regarded as a special, 17th electrode.

To measure the voltages due to excitation instead of impedances or currents, analog switch S1 is used rather than S2. The excitation current due to the sinusoidal excitation signal is first passed through the soft sensor system via MUX 1 and MUX 3. The resulting voltages are tapped by MUX 2 and passed on to an impedance converter, which in turn passes the signal to the final amplifier via S1.

Again, the insertion tool can be integrated as an alternative to the other 16 electrodes to measure the voltage. To measure its voltage, analog switch S3 is activated to couple the voltage derived via an intermediate impedance converter.

When processing the measurement data, care must be taken to ensure correction for the basic resistor's value R_{BR}. The necessity of this resistor lies both in the short-circuit protection of the circuit and its use as a known fixed reference resistor for calibration. To correct the impedance measurements, the impedance value that can be measured when MUX 1 and MUX 3 are switched to the same channel can be subtracted (this corresponds to the value of the base resistance). When measuring voltages, this base resistance manifests itself in the form of an offset, which is superimposed on every voltage measurement. This can be compensated for by reducing the voltage measurement values by the voltage measured at the electrode carrying the excitation current sink (active channel of MUX 3).

Finally, the microcontroller was used to enable communication between the signal electronics and a computer. The commands and measurement data are exchanged via a serial interface, that is, a universal serial bus (USB 2.0).

Special attention must also be paid to the parasitic capacitances of MUXs, as well as those of analog switches and

amplifiers [24]. In particular, with high-impedance sensor structures, their influences become noticeable at higher frequencies, which is especially disruptive when measuring voltages. Figure 4 illustrates this effect using a simplified circuit with few electrodes.
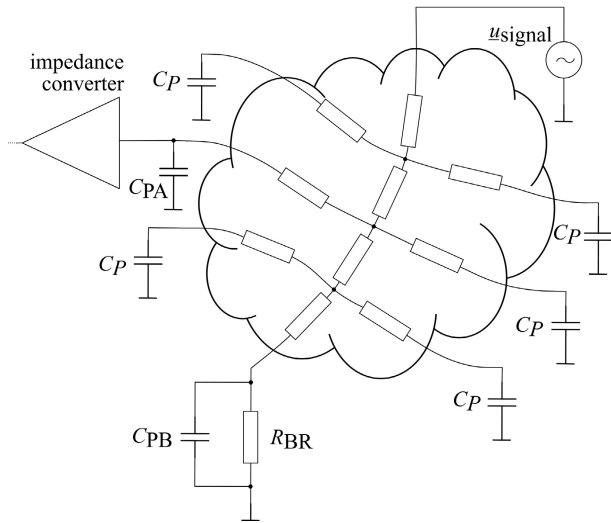

FIGURE 4. Simplified equivalent circuit of the influence of parasitic capacitances.

The parasitic capacitances at the individual electrodes are shown, which also depend on the switching state of the MUX. Deactivated channels have a parasitic capacitance of about $C_P = 60\,\text{pF}$, whereas active channels have parasitic capacitances of approximately $C_{PA} = 300\,\text{pF}$. Another parasitic capacitance of approximately $C_{PB} = 300\,\text{pF}$ is parallel to the base resistor. In general, the cross talk between channels is about $-60\,\text{dB}$.

An improvement of the measured values distorted by the parasitic capacitances can be achieved within the scope of signal processing, and in Chapter II-D, methods for this are proposed.

The complete circuit can be found in the supplementary material.

C. LEAKAGE CURRENT HANDLING

Leakage currents, which occur owing to the parasitic capacitance of the measurement channels shown in Figure 4, cannot be neglected in certain circumstances. For example, if high frequencies ($>10\,\text{kHz}$) are used in combination with high impedances ($>50\,\text{k}\Omega$) of the sensors, it may be necessary to consider them.

Depending on the application, different compensation strategies for leakage currents may be more advantageous than the others. For further consideration, the equivalent circuit of a single voltage divider to be measured is assumed, as shown in Figure 5. An initial rather simple variant for calculating a partially compensated voltage $\underline{u}_i^*$ is
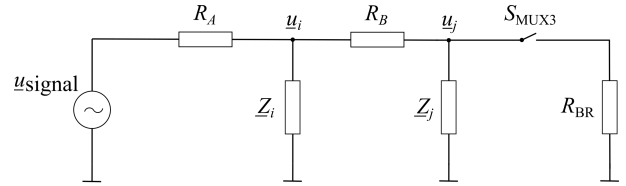

FIGURE 5. Equivalent circuit derived from the leakage current problem. The voltage to be determined $\underline{u}_i$ is accessed between the resistors R_A and R_B of the sensor material.

represented by

$$\underline{u}_i^* = \underline{u}_{\text{signal}} \frac{\underline{u}_i^{\text{closed}}}{\underline{u}_i^{\text{open}}} \tag{1}$$

where $\underline{u}_{\text{signal}}$ denotes the source voltage, and $\underline{u}_i$ denotes the voltage to be measured. The designations "open" and "closed" refer to the state of S_{MUX3} at which the voltages are determined. The impedances $\underline{Z}_i$ and $\underline{Z}_j$ correspond to parasitic capacitances. This corresponds to stretching the collapsed measurement voltage $\underline{u}_i$ (when S_{MUX3} is closed) to compensate for the voltage drop that already occurred before S_{MUX3} was closed, thereby referring it back to $\underline{u}_{\text{signal}}$ (comparisons of the application of this compensation strategy to uncompensated calculations by means of an EIT at different frequencies can be found in the supplementary material).

A slightly more sophisticated compensation, which also requires more measurements, is achieved by

$$\underline{u}_i^* = \underline{u}_{\text{signal}} \left(1 - \frac{\underline{u}_i^{\text{open}} - \underline{u}_i^{\text{closed}}}{\underline{u}_j^{\text{open}} - \underline{u}_j^{\text{closed}}} \right) \tag{2}$$

where $\underline{u}_j$ denotes the sink voltage. This results in

$$\underline{u}_i^* = \underline{u}_{\text{signal}} \frac{R_B \underline{Z}_i + R_A R_B}{(R_B + R_A)\underline{Z}_i + R_A R_B} \tag{3}$$

for the circuit shown in Figure 5. Thus, the influence of the R_{BR} and $\underline{Z}_j$ is removed. Moreover, as the influence of parasitic capacitance j decreases ($\underline{Z}_j \gg R_A, R_B$), the voltage obtained converges to the expected voltage of the pure, unloaded voltage divider. At higher frequencies, the influences of the parasitic capacitances becomes significant; however, the obtained voltage $\underline{u}_i^*$ is not exact, and the compensation via equation 1 tends to overcompensate in the case of a simple voltage divider. This compensation strategy is implemented within the firmware and can be enabled if required.

A compensation adapted to the network to be analyzed can provide better results for special problems with a known structure. In some cases, it may be necessary to completely solve the system of equations associated with the electrical network. However, compensation of the voltage drop due to an arrangement equivalent to a first-order low-pass filter can also be useful (such low-pass filters can occur because of parasitic capacitance C_p and the high resistance R_m of the measuring branches). For the low-pass transfer function

$H(j\omega) = \frac{1}{1+j\omega R_m C_p}$ it can be shown that

$$\frac{|H(j\omega)|}{\cos(\varphi(j\omega))} = 1 \qquad (4)$$

where j denotes the imaginary number, ω is the angular velocity corresponding to the frequency of the measuring signal, and $\varphi(j\omega)$ is the phase shift. Thus, the signal can be corrected by dividing by $\cos(\varphi(j\omega))$.

In EIT, parasitic capacitances can be considered by adjusting the boundary conditions of the electrodes to avoid errors. Therefore

$$\vec{n} \cdot (\sigma \nabla V) = -\upsilon_i V \text{ on } \partial\Omega_E \qquad (5)$$

holds as such an adapted boundary condition, with $\vec{n}$ as the normal vector of the boundary $\partial\Omega_E$, V is the electric potential, σ is the conductivity of the sensor material, and υ_i is the parameter representative of the admittance of the parasitic capacitances i (with $\sigma \nabla^2 V = 0$ in Ω describing electrostatics of the conductive sensing material). The parameters of parasitic capacitances must be calculated in advance or determined by calibration measurements.

D. FIRMWARE AND COMMUNICATION

The firmware of the ATMEGA 32U4 microcontroller was implemented in C++ [25] as a programming language using Microchip Studio (version 7.0.2542 with Atmel Kits (7.0.132), Microchip Technology, Chandler, Arizona, United States).

The core of the firmware is a superior class "Impedance-MultiSensingCircuit", which is mostly independent from the used microcontroller (for easier interchangeability of the controller) and provides all functionalities of the SIC. All components are accessible through the internal I^{2}C bus, which is why a "BUS" socket is provided on the outside of the housing, since an externally controlled operation of the SIC via the I^{2}C bus (reprogramming necessary) would theoretically also be possible. However, actual communication with a computer is enabled by a serial interface (USB 2.0) to achieve plug-and-play functionality (including automatic port scanning).

For faster transmissions, data are transmitted in binary form (32-bit floating point numbers, IEEE 754-1989), and information about the measurement mode and active measurement channels of each measurement is always transmitted as well to avoid errors when sending multiple measurement values sequentially.

The firmware performs self-calibrations as well as compensations of offsets independently and stores the calibration data on the electrically erasable programmable read-only memory (EEPROM) in case a calibration is not possible (an automatic calibration at start-up can only be performed if no sensors are connected to the SIC yet).

Because the standard frequency sweep application of the AD5933 usually does not make sense for the applications proposed in this work (instead of the entire frequency spectrum, measurements are often made at only one specific, advantageous frequency), the chip is misused in a different way. By repeatedly setting the AD5933's internal "repeat frequency"-flag, it is possible to rapidly measure at the same frequency over and over again.

Data acquisition and processing also occur within firmware. Compensation for the effects of the base resistance and partially those of the leakage currents can also be optionally enabled.

To accelerate extensive data acquisition (e.g., necessary for the evaluation of an EIT), it is possible to load stimulation and measurement patterns into EEPROM in advance. In this manner, the necessary measurement sequences are known to the SIC in advance, and time-consuming communication between individual measurements can be avoided. For example, EIT data can be streamed faster from SIC.

E. SOFTWARE

The software user interface for SIC was implemented as a class in Python [26] (version 3.9) and MATLAB [27]. This is intended to provide, in addition to the diverse data processing capabilities of these languages, easy handling with EIT software packages, such as PyEIT [28] or Eidors [29].

The main functionalities of the class are:

IMSC(): Default constructor.

begin(): Start command for establishing serial communication and calibrating the device.

sendStimPatternToHardware(): Transmission of the stimulation pattern stored under 'stimPattern' to SIC.

sendMeasPatternToHardware(): Transmission of the measurement pattern stored under 'measPattern' to SIC.

setFrequency(frequency): Sets the measurement frequency of the hardware [kHz].

gpioMode(port, value): Set the pin mode of a entire GPIO-port.

gpioRead(port): Reads and returns a entire GPIO-port.

gpioWrite(port, value): Writing pin-values of a entire GPIO-port.

measureCalib(): Reads the calibration data of SIC. The results are stored in the SIC object's calibration-values.

manual_Start_MeasurementOscillation(): Manual start of the AD5933 signal generator.

manual_Stop_MeasurementOscillation(): Manual stop of the AD5933 signal generator.

measureVoltage(fromEl, toEl, measEl, measureMode): Perform a voltage measurement at electrode 'measEl', where the electrode 'fromEl' is used as the signal source, and 'toEl' is used as the signal sink. Whether complex measurement values or only their magnitudes are determined can then be influenced by the 'measureMode'. The results are stored in the data object 'data' of the SIC object and additionally returned by the function itself.

voltageLeakageCorrection(onOff): Enable/disable hardware voltage leakage compensation for voltage measurements (according to equation 1).

measureImpedance(fromEl, toEl, measureMode): Impedance measurement between electrodes 'fromEl' and 'toEl'. Whether complex measurement values or only their magnitudes are determined can then be influenced by the 'measureMode'. The results are stored in the data object 'data' of the SIC object and additionally returned by the function itself.

measureAll(measureMode): Measures all possible voltages and impedances between the electrodes and needle of the SIC (136 impedance and 2601 voltage readings). Whether complex measurement values or only their magnitudes are determined can then be influenced by the 'measureMode'. The results are stored in the data object 'data' of the SIC object.

measureEIT(measureMode): Measures the voltage magnitudes defined by 'measPattern', which are caused by the excitation defined by 'stimPattern' ('measPattern' and 'stimPattern' must be loaded onto the SIC in advance). This is particularly interesting for EIT measurements or fast measurement sequences. The measurement value compensation can be activated via 'measureMode' (according to Equation 1). The results are stored in the data object 'data' of the SIC object.

Besides these functions, the data class of the SIC object for storing past measurements is also noteworthy.

data Data object that stores past measurements in a structured manner. In addition to the type of measured value ('impedances', 'voltages', 'eit', 'other'), information about the signal source ('fromElectrode'), signal sink ('toElectrode'), measuring electrode ('measureElectrode'), real component ('realValue'), imaginary component ('imagValue'), and magnitude ('magnitude') are also stored. When using 'measureAll(...)' or 'measureEIT(...)', the data object is reinitialized before the start of the measurement.

More detailed descriptions were provided in the code itself or by calling the respective help in Python or MATLAB.

III. RESULTS
A. HARDWARE MODULE
The final hardware of the SIC (Figure 6) is protected by a carbon fiber-reinforced 3D-printed casing (CarbonFil, Formfutura BV, Nijmegen, Netherlands) with an integrated elastic shock absorber (TPU 95A, Ultimaker BV, Utrecht, Netherlands), the dimensions (L × W × H) are 88 mm × 76 mm × 18 mm and the weight is 120 g. On the top side (Figure 6a) are the connectors for the 16 electrodes ('MEAS'), an optional 17th electrode ('NEEDLE'), digital inputs/outputs ('GPIO1', 'GPIO2', 'GPIO3'), the I^{2}C bus including power supply ('BUS'), and the status LEDs ('LED'). Inside (Figure 6b), the printed circuit board (PCB) is visible, where the left third of the PCB can be cut off at the white line if further miniaturization is required (external oscillator, bus connection and small breadboard for optional extensions are

omitted), whereby the minimum dimensions of (L × W) 55 mm × 59 mm can be achieved (connection via micro USB, standard EN 62684:2011). The total cost of the components was less than 100 \$ (United States dollar).

The power consumption of the module was tested under various conditions (5 V USB supply voltage). For initialization, 400 mW was measured, while 315 mW was required in standby mode. In addition, 335 mW was obtained during EIT measurements, 385 mW during continuous impedance measurements, and 390 mW during continuous voltage measurements. In addition, the power consumption can be increased by loads on the GPIO, the influence of the impedances of the sensors to be measured is < 10 mW.
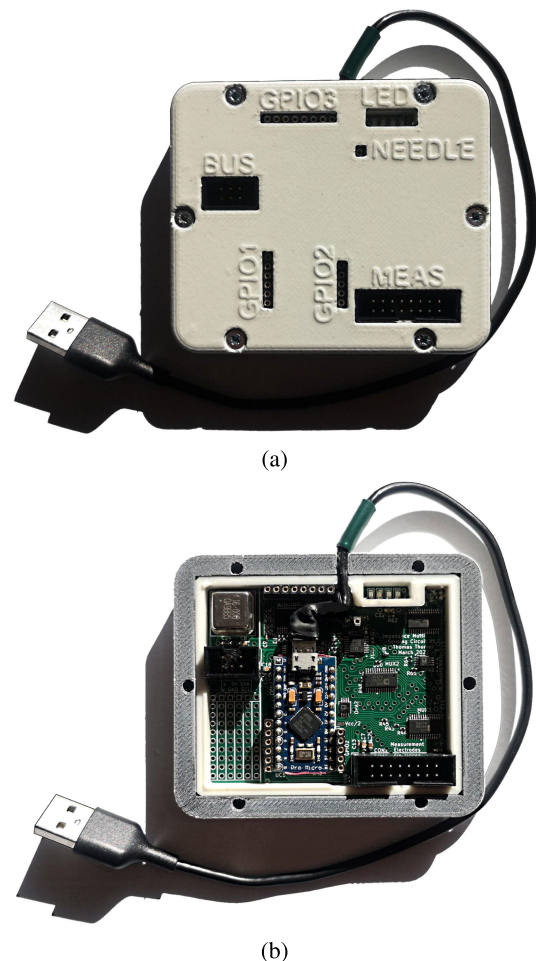

(a)

(b)

FIGURE 6. Complete measuring box; (a) closed, (b) open.

B. SOFTWARE INTERFACE
The entire software interface was implemented as a single Python or MATLAB class, which only needs to be initialized once when used. Subsequently, measurements or measurement sequences can be performed using command calls. The measurement time of single measurements (4 ms in Python, 15 ms in MATLAB) can be shortened by measurement sequences (<3.6 ms per sample reachable).

C. ACCURACY

To evaluate the accuracy of the SIC, comparative measurements were performed using a digital multimeter (Keysight 34465A, Keysight Technologies, Inc., Santa Rosa, California, USA) with a relative accuracy (with respect to full scale) of $\leq 0.04\,\%$ with respect to AC voltage measurements and $\leq 0.0025\,\%$ with respect to resistance measurements.

The basic accuracy of the voltage measurement (Figure 7a, where $\mathrm{normV}(\underline{U}) = \left| \frac{U - U_{\mathrm{BR}}}{U_0 - U_{\mathrm{BR}}} \right|$) was determined by measurements on a simple voltage divider ($\sum R = 500\,\Omega$, frequency f of 2 kHz), resulting in a standard deviation of the relative measurement error of $8.1505 \cdot 10^{-05}$ (with respect to the full scale) with a corresponding mean of $-1.7048 \cdot 10^{-05}$. Furthermore, Figure 7a proves the linearity of the voltage measurement.

A comparison of the measured and theoretically calculated phase shifts of a filter is shown in Figure 7b. Therefore, the filter used is a simple RC low-pass filter (resistor R, capacitor C), considering the base resistance R_{BR} of the SIC, resulting in $G(j\omega) = \frac{R_{\mathrm{BR}} C s + 1}{(R_{\mathrm{BR}} C + RC)s + 1}$ as transfer function. The exact component values, which were also used for the calculation, were determined with the digital multimeter to be $R = 2100\,\Omega$, $C = 3.28\,\mathrm{nF}$ and $R_{\mathrm{BR}} = 428\,\Omega$.

The accuracy of the resistance measurement was determined using resistors of four different scales ($0 - 500\,\Omega$, $0 - 5\,\mathrm{k}\Omega$, $0 - 50\,\mathrm{k}\Omega$, $0 - 500\,\mathrm{k}\Omega$, 32 samples each linearly distributed) at three different frequencies (2 kHz, 10 kHz and 100 kHz). Results of the relative error $\mathrm{error}_{\mathrm{R,rel}} = \frac{R_{\mathrm{KEYSIGHT\ 34465A}} - R_{\mathrm{SIC}}}{R_{\mathrm{fullScale}}}$ are shown in Figure 7c as standard deviations and in Figure 7d as the mean values. The signal attenuation due to parasitic capacitances by increasing the sample resistance (voltage dividers with $\sum R = 500\,\Omega$, $5\,\mathrm{k}\Omega$, $50\,\mathrm{k}\Omega$, and $500\,\mathrm{k}\Omega$) as well as increasing the frequency ($2 - 100\,\mathrm{kHz}$) is shown in Figure 7e.

D. APPLICATION EXAMPLES

Some examples of applications were tested to demonstrate the applicability of SIC. The sensor material used was a carbon black-silicone composite based on Ecoflex 35 Fast (Smooth-On, Inc., Macungie, PA, USA) with 7.5 wt% carbon black (XPB 545 POWDER from ORION Engineered Carbons GmbH, Frankfurt, Germany), whose exact composition and preparation were described by Thurner et al. [7].

To demonstrate the applicability as a strain gauge or compression element, tensile and compression tests were carried out (Figure 8). Thereby, a uniaxial testing machine (Zwick Z005, Zwick/Roell GmbH & Co. KG, Ulm, Germany) including a force transducer (Zwick/Roell Xforce HP 200 N, Zwick/Roell GmbH & Co. KG, Ulm, Germany), which meets the criteria of accuracy classes according to ISO 7500-1, was used. The results showed the piezoresistive behavior typical for carbon black silicone composite [30].

Figure 9 shows the results of a simple position detection method for an inserted needle to determine the location of
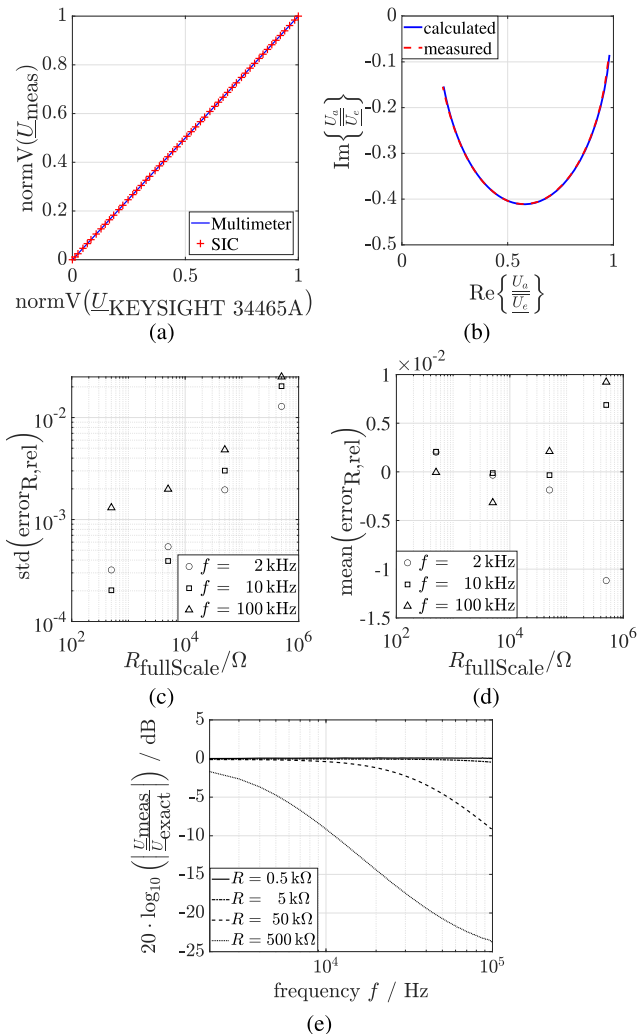

FIGURE 7. Accuracy of SIC module; (a) Measured voltage of the SIC in comparison to the measured voltage of the multimeter, (b) measured transmission behavior of an analog filter, shown on the complex plane, compared to the theoretically calculated model, (c) accuracy of resistance measurements, represented by the standard deviation of the relative error with respect to the full scale values, (d) accuracy of resistance measurements, represented by the mean deviation of the relative error with respect to the full scale values, (e) Measurement voltage drops due to parasitic capacitances of the measurement circuitry.

penetration. The implementation corresponds to Figure 1b, where the evaluation of the needle position corresponds to the tapped voltage from two sensor layers, each forming an electrical gradient field. The detection area was 32 mm × 32 mm, and the measurement frequency was 2 kHz. Determination of position detection accuracy revealed a mean error and standard deviation of $2.74 \pm 1.07\,\%$ related to the entire detection area.

An example of grid-shaped tactile position sensors and their evaluation is shown in Figure 10 (according to the sensor principle of Figure 1g using Ecoflex 35 Fast as the silicone filler between the conductive structures). In x and y direction eight strings each were used. Only the shape and location of the deformations were captured in this case, and an accurate quantitative pressure evaluation was not

(a)   (b)

(c)

(d)
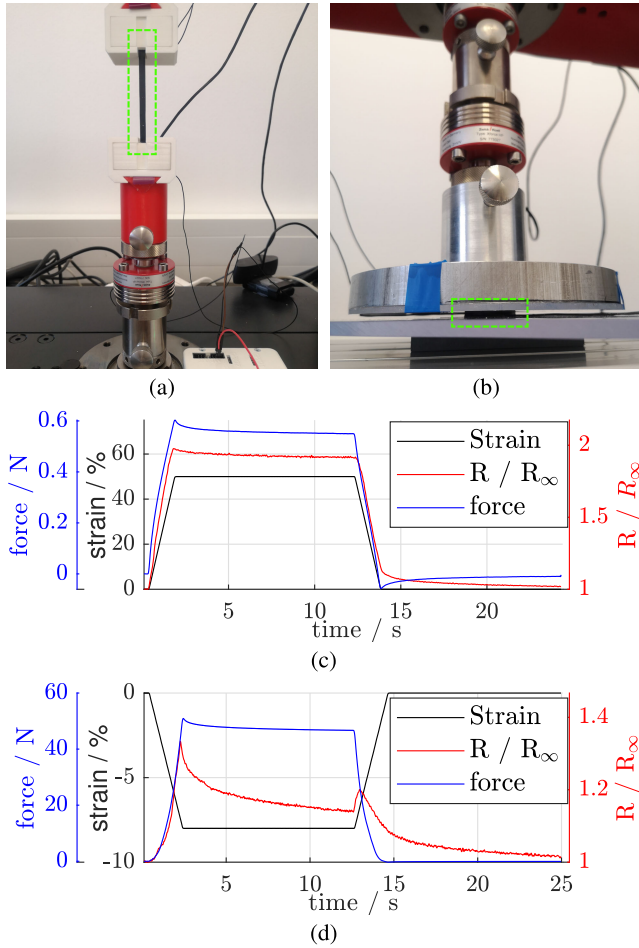
FIGURE 8. Soft carbon black silicone composite strain gauge and pressure element application: Strain specimen (a) and pressure element (b) during measurement (specimen highlighted in green for better visibility), measurement results of strai n (black), force (blue) and measured relative resistance R/R_∞ (red) of strain gauge (c) as well as pressure element (d).

intended. For evaluation, the resistances (signal frequency of 100 kHz) of the individual strings in the x-direction $R_{x_i,t}$ and y-direction $R_{y_i,t}$ at time t were used for calculation of the indicator variables $\zeta_{i,j}$ as

$$\zeta_{i,j} = \frac{\left(R_{x_i,t} - R_{x_i,\kappa}\right)\left(R_{y_j,t} - R_{y_j,\kappa}\right)}{\left(R_{x_i,\kappa} + R_{y_j,\kappa}\right)^2} \quad (6)$$

where $R_{x_i,\kappa} = 0.8\,R_{x_i,\kappa} + 0.2\,R_{x_i,t-1}$ and $R_{y_j,\kappa} = 0.8\,R_{y_j,\kappa} + 0.2\,R_{y_j,t-1}$ apply. Two different scenarios were chosen for demonstration: A large scale compression covering nine cells (Figures 10a and 10b), and a single cell compression with simultaneous stretching of the entire sensor array (Figures 10c and 10d). The pressure on the sensor system to generate the detection examples shown in Figure 10 was applied uniformly from both sides using two identical rigid stamps in each case (applied pressure of 20 kPa was introduced by pliers with adjusted spring, see Figure 10b and 10d). Changes due to the stretching of the mat itself were suppressed by the algorithm.
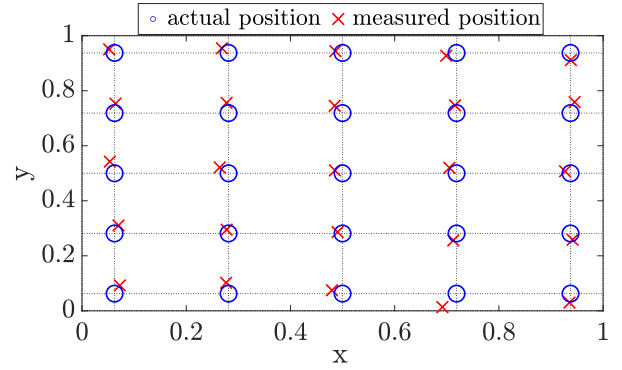

FIGURE 9. Results of a 1.5D position detection by using double layer sensor mats according to figure 1b. A comparison of actual and measured positions as normalized coordinates is shown.

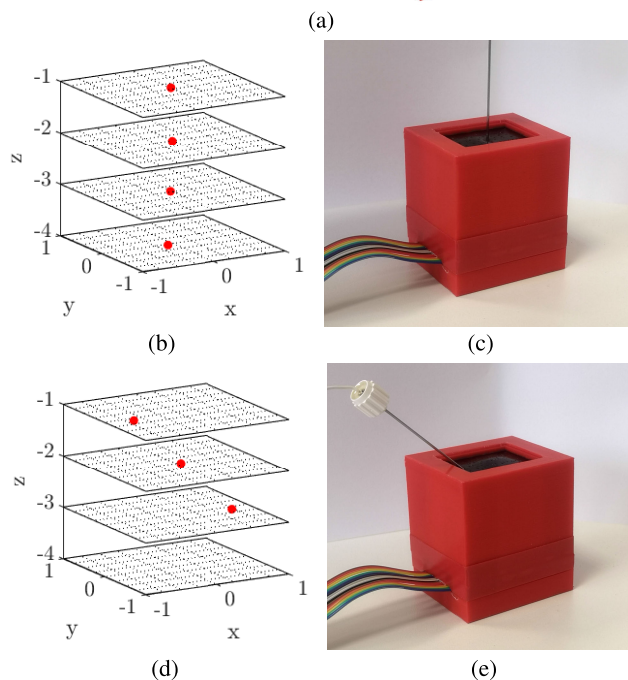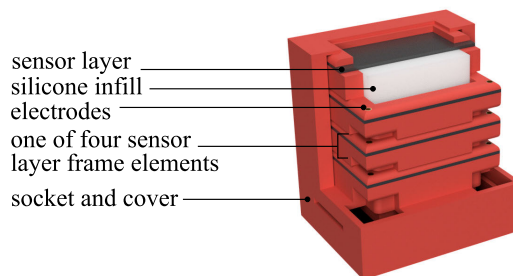(a)   (b)

(c)   (d)
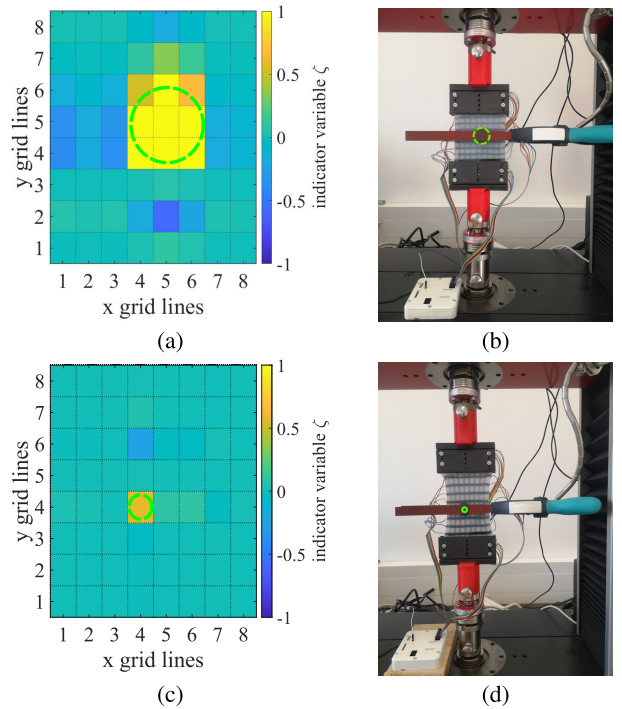
FIGURE 10. Grid deformation position detection. Abscissa and ordinate represent the numbers of the x- and y-strings respectively, the color bar shows the indicator variable ζ, which indicates changes in the conductivity of the strings at their crossing points (cells) due to compression. The real pressure regions are shown dashed in green, (a) shows the evaluation of a larger, nine cells covering circular compression, (b) shows the unstretched sensor mat under load measured thereby, (c) shows the evaluation of a small single cell compression of the sensor system in a stretched state (40 % strain) and (d) shows the stretched sensor mat under load measured in this case.

The resistivity distribution of a sensor layer reconstructed with EIT, according to the sensor principle shown in Figure 1h, is shown in Figure 11. Deformations or compressions of the sensor mat due to external forces can be detected. Ecoflex 35 Fast was placed underneath the sensor mat as a soft base, and differently shaped rigid stamps were pressed onto the sensor mat by applying a pressure of 20 kPa to produce the examples shown in Figure 11. Eidors [29]
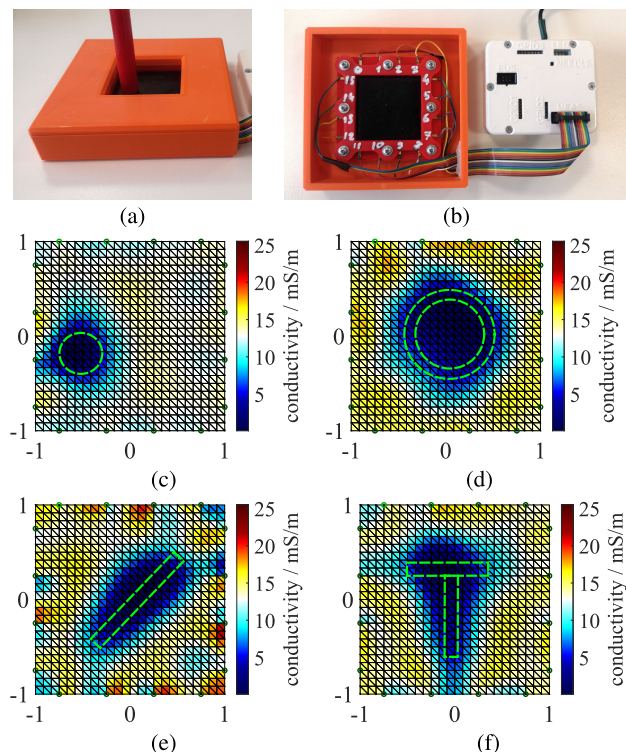
FIGURE 11. EIT reconstruction of resistivity distribution. The measurement setup under load is shown in (a), the opened setup as well as the sensor interface in (b). For the reconstruction results, abscissa and ordinate represent respectively the normalized x- and y-coordinates of the sensor layer, the colorbar shows the reconstructed conductivity of the layer. The measuring electrodes are indicated by dark green dots at the borders of the images. The geometry of the true deformation is shown dashed in green. Compression of the sensor mat by a (c) small cylinder, (d) hollow cylinder, (e) I-shaped body, (f) T-shaped body.

FIGURE 12. Multilayer arrangement for exploring the third dimension: sensor arrangement (a), measurement results (b) when positioning a needle according to (c), measurement results (d) when positioning a needle according to (e).

was used for the calculations. The measurement signal frequency was 100 kHz, and leakage current compensation was enabled during the measurements. A single point position detection mean error and standard deviation of 6.0 ± 2.6 % was recorded. The minimum measurable load was 0.35 N on a cylindrical object of 6 mm diameter. As an example to access the third dimension, measurements were performed according to Figure 1d. Four 2D sensor mats were stacked above each other (Figure 12). The approach and algorithm of the individual layers for 2D position detection corresponded to that of Thurner et al. [7]. A conductive needle was used to determine the resistance of the sensor mats between the needle and the corner electrodes. The position was determined using triangulation and correction functions. However, the entire electronics were replaced by the proposed Sensor Interface Module. The accuracy of the system was characterized by the accuracy of the individual sensor layers. In relation to the entire detection range (pin spacing 30 mm ×40 mm), a mean error and standard deviation of 4.42 ± 2.67 % was determined (using a 9 × 7 grid with 4 mm spacing). In the central region of the sensor layer (15 mm ×20 mm) even an accuracy of 1.48±0.68 % could be achieved.

In addition, the supplementary material contains videos for the presented applications.

IV. DISCUSSION

The demand for the sensory interface presented here is motivated by the acceleration of development of new low-cost hybrid surgical simulators. Owing to the universality of the developed module, it supports various soft sensor principles. For example, the sensor interface can handle most flexible and stretchable piezoresistive sensors according to the survey of recent sensors by Duano et al. [13]. Further more, the module could completely replace the evaluation electronics of simulators, such as that used for simulating laryngeal pacemaker implantation [7] (2D position detection). This can increase accuracy and robustness of measurements (in [7] the mean error could be reduced from 3.51 ± 1.64 % to 1.48 ± 0.68 % for the central region), but also enables improved tool tracking, such as in simulators for epidural anesthesia [31], [32].

Simulators, such as the one for injection laryngoplasty training from Lee et al. [33] or the one for basic microsurgery training at the arteries, veins and nerves from Alser et al. [34], could greatly benefit from soft sensing. In addition, methods such as anastomosis [35], [36] could also benefit from the possibility of quantitative feedback (measured resistance of structures can show quality of connection).

Although some of the sensor principles mentioned are already used in industry [13], such as collision detectors in robots [11], [18], conventional industrial sensors cannot be used in surgical simulators. Solid components, which usually occur somewhere, distort the haptics of soft, synthetic tissue. In surgical simulations, entirely soft sensors, sometimes stretchable, are required. These tactile properties of such sensors, however, result in additional requirements for the evaluation electronics. The avoidance of contact resistance between electrodes and soft carbon black silicone composites [7], for example, is greatly improved using AC voltage signals. Furthermore, numerous four-wire impedance measurements are possible because to the large number of electrodes. In addition, the data evaluation via AD5933 corresponds to a notch filter, whereby noise is further suppressed.

According to Adler et al. [20, p. 61], there are two ways to reduce the effect of parasitic capacitances (visible by the higher-frequency measurements in Figure 7e), either by hardware improvements to compensate for these capacitances or by reducing their influence on the result by considering the real and imaginary parts of the measurements, because the capacitances lead to a phase shift of the signal. Alternatively, compensation through the structure of the evaluated network is also possible. Because hardware adaptations by impedance converters [37], [38] would be associated with high additional costs, the problem of parasitic capacitances is to be improved by adapted signal processing within the scope of this work. Figure 11 demonstrates that even not fully accurate corrections, such as those from Equation 1, can give useful results in EIT. The fact that the hollow cylinder in Figure 11d was not reconstructed hollow was due to the reconstruction algorithm and not due to the accuracy of the measurement system, which can be verified by simulations (see supplementary material). Even better is the avoidance of such leakage effects by sensor structures with lower impedances or by the use of lower frequencies. However, reducing the frequency of the signal generator also leads to more difficult conditions when the signal is coupled into the sensor system.

The ability to flexibly measure voltages and/or impedances depending on the task as well as the 17th electrode are also unique features. Although seemingly trivial, the 17th electrode enables the position detection of an electrically conductive tool within a sensor layer, combined with the applicability of a 16-channel EIT. This can be used, for example, to compensate for deviations in the position detection of the tool caused by deformations of the sensor mat and thus to suppress their effects. In general, the application of detecting a voltage carrying tool introduced into a sensor system is

of great importance for surgical simulators. An extension of such sensor systems into the third dimension could also be demonstrated. The sensor interface in combination with soft sensors thus provides a cost-effective method for relative tool tracking within surgical simulators in up to three-dimensional space.

The accuracy of the module, which has already been documented in Section III-C, shows sufficiently accurate results for use in surgical simulators. It was shown that the deviations of the voltage measurements and their linearity (Figure 7a) were in the range of the reference instrument's accuracy tolerance, and the measured phase shifts (Figure 7b) were almost identical. The resistance measurements showed standard deviations of less than 0.5 %, as well as tolerable systematic deviations (mean error below 0.3 %, Figure 7d) for the resistance ranges relevant to the use of the module with carbon black silicone composites ($< 50 \, \text{k}\Omega$). The results of the application examples from Section III-D demonstrate that the achieved accuracies are sufficient for the intended applications, and good results can be achieved.

The data acquisition speed is also sufficient; in the fastest mode, acquisition of 208 readings for the EIT is possible in less than one second (about five times faster than the 16-channel low-cost EIT circuit of Zamora-Arellano et al. [39]). Owing to the electromechanical properties of carbon black silicone composites [40], [41], concerning both the piezoresistivity and creep of the viscoelastic material, faster sampling is not necessary because resistance changes are somewhat persistent and thus do not disappear immediately when the material is unloaded.

Direct comparison to other systems is difficult because the requirements are specific and yet extensive. A measurement system with all the necessary requirements for the presented sensor technology in surgical simulators has not yet been found. Furthermore, research groups in similar disciplines often use commercially available data acquisition systems for measurements (e.g. soft E-skin tactile sensing [14], [15], strain mapping sensor by EIT [42], or tactile EIT sensors [18], [43], [44], [45]). Such systems are deliberately not used because they are neither cheap nor small and rarely portable. In addition, the measurement module proposed fulfills additional essential functions, as previously mentioned.

In many other cases, highly specialized circuits with little flexibility are used, which prevents more universal usage (e.g., resistance measurements of sensor arrays [14], [15], DC based smart skin sensors [11], [12], or specialized EIT systems [46], [47], [48], [49]).

However, partial functions can be compared, especially in the field of electrical impedance tomography, since such circuits operate with a similar number of measurement channels and need to measure voltages and inject currents at the same time. Although there are already some comparable EIT modules of other research studies, many of them suffer from serious disadvantages regarding their application within surgical simulators. Reasons for this include too few electrodes,

TABLE 1. Comparison of most relevant EIT solutions for use in surgical simulators.

	Wu et al. [19]	Zamora et al. [39]	Chen et al. [48]	Liu et al. [49]	proposed system
Accuracy: single point position detection error	$< 11\%$	n. a.	$3.8 \pm 2.3\%$	n. a.	$6.0 \pm 2.6\%$
ADC resolution	16 bit	24 bit	16 bit	14 bit	12 bit
EIT-frame time consumption	n. a.	~ 5 s	~ 0.6 s	n. a.	~ 1 s
Signal frequency	DC	$4 - 80$ kHz	$10 - 50$ kHz	60 kHz, 100 kHz	$2 - 100$ kHz
Number of electrodes	16	16	16	16	17
Additional channels	n. a.	n. a.	n. a.	n. a.	19 GPIO-pins
Price	> 1000 \$	100 \$	n. a.	> 440 \$	100 \$
Dimensions of circuit board	n. a.	n. a.	116 mm $\times$ 75 mm	n. a.	59 mm $\times$ 55 mm
Additional required hardware	Computer, data acquisition card National Instruments USB-6210, DC power supply	Computer, DC power supply	Computer	Computer, Red Pitaya STEMLab 125-14 development board	Computer
Required Software	Python / pyEIT	Matlab / EIDORS or GNU Octave	n. a.	n. a.	Python / pyEIT or Matlab / EIDORS
Portable	Hardly	Yes	Yes	Yes	Yes
Open Source	No	No	No	No	Yes
Suitable for surgical simulators	No	No	Partly	No	Yes
Additional comments	Several separate components			Several separate components	Leakage current compensation available

as in Zhang et al. [46], systems that are too slow, as in Pitaloka et al. [47], or DC usage, as in Park et al. [18] or Lee et al. [50], resulting in more difficult signal coupling into the soft carbon black silicone composite. In addition, leakage currents owing to parasitic capacitances or their compensation are rarely discussed, which is especially relevant for low-cost systems because the hardware components are less accurate.

Most relevant EIT systems regarding an application in surgical simulators (research from Wu et al. [19], Zamora-Arellano et al. [39], Chen et al. [48], and Liu et al. [49]) were compared by Table 1 (accuracy specified as relative mean error $\pm$ standard deviation from total sensors detection range, not available information is marked as n. a.).

Sensitivity of EIT systems to applied force is strongly dependent on the used sensor material. Zhu et al. [51] provided an overview of the sensitivity of various soft, flexible materials in the field of tactile sensing. For the proposed system, the limit of measurability using the carbon black silicone sensor layer with EIT was a force of 0.35 N.

Additional relevant work was compared to obtain an better overview of the accuracy of similar sensor systems. Yoshimoto et al. [52] could achieve an accuracy of $5.7 \pm 2.8\%$ for position detection, and local pressure detection with error in the range of $0.027 - 0.051$ N/mm^2 with their tomographic tactile electromechanically coupled conductor sensor system. Avery et al. [44] were able to achieve an overall accuracy of $7.7 - 15.3\%$ for various perturbation diameters with their tactile EIT sensor. For comparison with a deep neural network-based system, Park et al. [53] obtained an error of $4.9 \pm 2.8\%$ for their large area robotic tactile sensing system.

Away from EIT systems, a comparison to other tactile sensor systems is also useful. O'Neill et al. [12] designed a tactile sensor, similar to Figure 1c, in which an additional conductive layer is punctually pressed onto the underlying layer (instead of a surgical tool) to enable position detection (average error of 7.8 %). The dual layer flexible annular sectorial sensor by Wu et al. [11] achieved a detection error of about 4 % by measuring constant electric fields. For sensor arrays such as those of Fu et al. [15] or Müller et al. [14], the measurement accuracy depends on the distance between the individual elements, down to 1 mm for the latter. Schao et al. proposed a general tactile sensor system [54], which can be extended to any number of sensors, but only allows simple DC resistance and capacitance measurements. Furthermore, the possibility of four-wire measurement, voltage or current injection, or EIT capabilities are missing for the intended use within surgical simulators. However, this comparison should not detract from the fact that all these works do not offer the required range of functions for surgical simulators.

The strengths of the SIC module are its low cost and sufficient accuracy for use with soft carbon black silicone composites. Using AD5933, the data acquisition corresponds to a notch filter, which drastically reduces interference. The portability (can even be operated via smart phones using USB adapters) and universal applicability also play important roles. The disadvantages are the much more impactful parasitic capacitances compared to more precise and expensive systems, as well as the leakage currents caused by them. This limits the application either to low impedance sensors (< 50 kΩ) or lower frequencies (< 10 kHz).

The ATMEGA 32U4 is sufficient for the proposed sensor interface module because the AD5933 handles most of the signal processing, including DFT. The microcontroller thus mainly controls the multiplexers and analog switches and serves as a communication element between the indi-

vidual internal components. Code and memory consumption have been implemented compactly and strongly utilize the ATMEGA 32U4 (80 % program memory consumption). A more powerful micro controller is however not necessary, as the ATMEGA 32U4 offers all the necessary advantages such as miniaturization, low power consumption and USB support. In case more resources would be needed, external control by another controller via the I^{2}C bus is possible.

Improvements to the system could be achieved by using AD5941 (Analog Devices Inc., Norwood, Massachusetts, United States) instead of AD5933. This offers an ADC resolution of 16 bits, a larger frequency range for the sensing signal, and the ability to set the number of samples used for the DFT. In addition, faster data rates could be achieved in the module via the Serial Peripheral Interface (SPI). Increasing the baud rate of the serial interface (USB) would also lead to an acceleration of the sampling rate (the timing of the SIC module: serial communication 1.2 ms, I^{2}C communication 1.3 ms, Data measurement AD5933 1 ms).

The scientific contribution of the proposed sensor interface including the sensor principles can be concluded by three major aspects. First, the sensor interface serves as a cost-efficient base module to greatly accelerate the future development of hybrid surgical simulators, as the module meets their specific requirements. Such simulators are important because they improve the skills of novice surgeons and thus minimize the risk of surgical procedures on patients [2]. Second, several principles were demonstrated how up to three-dimensional tool tracking and deformation or force detection can be implemented in surgical simulators without distorting the realistic haptics of the patient phantoms (essential according to [4]). Third, challenges in the use of low-cost measurement electronics within this application area were identified and solutions were presented and implemented (capacitive coupling of signals to avoid contact resistances, leakage current compensation, etc.).

Finally, it should be mentioned that all circuits and their files, CAD files, firmware, and software are published as open sources in the supplementary material as well as via GitHub [55] to make access to the module as simple and straightforward as possible.

V. CONCLUSION

The presented sensory interface circuit is a universal tool for easy handling of soft sensors in hybrid surgical simulators. A miniaturized, low-cost circuit with Python and MATLAB software interface was developed to cover essential core features, such as low price, universal applicability, and simple handling. The module is USB-driven, has 17 measurement channels as well as GPIO pins, and is capable of complex impedance and voltage measurements between all measurement channels. It has been optimized for the use of soft carbon black silicone composites as conductive sensor materials.

The module allows the evaluation of various soft sensors, from simple strain gauges or pressure elements to flat multilayer arrangements for multi-dimensional position detection of inserted conductive objects, up to electro-impedance tomography of conductive structures.

To maximize the benefit for the development of future simulators, all necessary files such as circuits, firmware and software as source code, as well as CAD data, are provided.

REFERENCES

[1] S. S. Y. Tan and S. K. Sarker, "Simulation in surgery: A review," *Scottish Med. J.*, vol. 56, no. 2, pp. 104–109, 2011.

[2] S. R. Dawe, G. N. Pena, J. A. Windsor, J. A. J. L. Broeders, P. C. Cregan, P. J. Hewett, and G. J. Maddern, "Systematic review of skills transfer after surgical simulation-based training," *Brit. J. Surg.*, vol. 101, no. 9, pp. 1063–1076, Jul. 2014.

[3] A. J. Lungu, W. Swinkels, L. Claesen, P. Tu, J. Egger, and X. Chen, "A review on the applications of virtual reality, augmented reality and mixed reality in surgical simulation: An extension to different kinds of surgery," *Exp. Rev. Med. Devices*, vol. 18, no. 1, pp. 47–62, Jan. 2021.

[4] K. Rangarajan, H. Davis, and P. H. Pucher, "Systematic review of virtual haptics in surgical simulation: A valid educational tool?" *J. Surgical Educ.*, vol. 77, no. 2, pp. 337–347, Mar. 2020.

[5] R. M. Viglialoro, N. Esposito, S. Condino, F. Cutolo, S. Guadagni, M. Gesi, M. Ferrari, and V. Ferrari, "Augmented reality to improve surgical simulation: Lessons learned towards the design of a hybrid laparoscopic simulator for cholecystectomy," *IEEE Trans. Biomed. Eng.*, vol. 66, no. 7, pp. 2091–2104, Jul. 2019.

[6] S. Teodoro-Vite, J. S. Pérez-Lomelí, C. F. Domínguez-Velasco, A. F. Hernández-Valencia, M. A. Capurso-García, and M. A. Padilla-Castañeda, "A high-fidelity hybrid virtual reality simulator of aneurysm clipping repair with brain sylvian fissure exploration for vascular neurosurgery training," *Simul. Healthcare, J. Soc. Simul. Healthcare*, vol. 16, no. 4, pp. 285–294, 2021.

[7] T. Thurner, B. Esterer, D. Furst, M. Hollensteiner, S. Sandriesser, P. Augat, E. Pruckner, D. Wirthl, M. Kaltenbrunner, A. Muller, G. Förster, C. Pototschnig, and A. Schrempf, "Smart artificial soft tissue—Application to a hybrid simulator for training of laryngeal pacemaker implantation," *IEEE Trans. Biomed. Eng.*, vol. 70, no. 2, pp. 735–746, Feb. 2023.

[8] L. Wang, T. Ding, and P. Wang, "Thin flexible pressure sensor array based on carbon black/silicone rubber nanocomposite," *IEEE Sensors J.*, vol. 9, no. 9, pp. 1130–1135, Sep. 2009.

[9] M. E. Spahr, R. Gilardi, and D. Bonacchi, "Carbon black for electrically conductive polymer applications," in *Fillers for Polymer Applications*. Berlin, Germany: Springer, 2016, pp. 375–400.

[10] J. Shintake, Y. Piskarev, S. H. Jeong, and D. Floreano, "Ultrastretchable strain sensors using carbon black-filled elastomer composites and comparison of capacitive versus resistive sensors," *Adv. Mater. Technol.*, vol. 3, no. 3, Mar. 2018, Art. no. 1700284.

[11] H. Wu, H. Wang, J. Huang, Y. Zhang, and J. Ye, "A flexible annular sectorial sensor for detecting contact position based on constant electric field," *Micromachines*, vol. 9, no. 6, p. 309, Jun. 2018.

[12] J. O'Neill, J. Lu, R. Dockter, and T. Kowalewski, "Stretchable, flexible, scalable smart skin sensors for robotic position and force estimation," *Sensors*, vol. 18, no. 4, p. 953, Mar. 2018.

[13] L. Duan, D. R. D'hooge, and L. Cardon, "Recent progress on flexible and stretchable piezoresistive strain sensors: From design to application," *Prog. Mater. Sci.*, vol. 114, Oct. 2020, Art. no. 100617.

[14] V. Mueller, C. Urbahn, R. M. Al-Gaifi, M. Schmidt, J. Saenz, and N. Elkmann, "Tactile sensor modules for flexible manipulation," in *Proc. 50th Int. Symp. Robot.*, Jun. 2018, pp. 1–7.

[15] Y.-F. Fu, F.-L. Yi, J.-R. Liu, Y.-Q. Li, Z.-Y. Wang, G. Yang, P. Huang, N. Hu, and S.-Y. Fu, "Super soft but strong e-skin based on carbon fiber/carbon black/silicone composite: Truly mimicking tactile sensing and mechanical behavior of human skin," *Compos. Sci. Technol.*, vol. 186, Jan. 2020, Art. no. 107910.

[16] W. Zhai, Q. Xia, K. Zhou, X. Yue, M. Ren, G. Zheng, K. Dai, C. Liu, and C. Shen, "Multifunctional flexible carbon black/polydimethylsiloxane piezoresistive sensor with ultrahigh linear range, excellent durability and oil/water separation capability," *Chem. Eng. J.*, vol. 372, pp. 373–382, Sep. 2019.

[17] H. Lee, K. Park, J. Kim, and K. J. Kuchenbecker, "Internal array electrodes improve the spatial resolution of soft tactile sensors based on electrical resistance tomography," in *Proc. Int. Conf. Robot. Autom. (ICRA)*, 2019, pp. 5411–5417.

[18] K. Park, H. Park, H. Lee, S. Park, and J. Kim, "An ERT-based robotic skin with sparsely distributed electrodes: Structure, fabrication, and DNN-based signal processing," in *Proc. IEEE Int. Conf. Robot. Autom. (ICRA)*, May 2020, pp. 1617–1624.

[19] H. Wu, B. Zheng, H. Wang, and J. Ye, "New flexible tactile sensor based on electrical impedance tomography," *Micromachines*, vol. 13, no. 2, p. 185, Jan. 2022.

[20] A. Adler and D. Holder, *Electrical Impedance Tomography: Methods, History and Applications*. Boca Raton, FL, USA: CRC Press, 2021.

[21] L. Zou, C. Ge, Z. Wang, E. Cretu, and X. Li, "Novel tactile sensor technology and smart tactile sensing systems: A review," *Sensors*, vol. 17, no. 11, p. 2653, Nov. 2017.

[22] Y. D. Jiang and M. Soleimani, "Capacitively coupled electrical impedance tomography for brain imaging," *IEEE Trans. Med. Imag.*, vol. 38, no. 9, pp. 2104–2113, Sep. 2019.

[23] M. Takhti and K. Odame, "Structured design methodology to achieve a high SNR electrical impedance tomography," *IEEE Trans. Biomed. Circuits Syst.*, vol. 13, no. 2, pp. 364–375, Apr. 2019.

[24] A. M. M. da Mata, B. F. de Moura, M. F. Martins, F. H. S. Palma, and R. Ramos, "Parasitic capacitances estimation of an electrical impedance tomography data acquisition system by Bayesian inference," *Measurement*, vol. 174, Apr. 2021, Art. no. 08992.

[25] ISO Central Secretary. *Programming Languages—C++*. Int. Org. Standardization, Geneva, CH, USA, Standard ISO/IEC 14882, 2020. [Online]. Available: https://www.iso.org/standard/79358.html

[26] R. G. Van Rossum and F. L. Drake, *Python Reference Manual*, vol. 10. Scotts Valley, CA, USA: CreateSpace, 2009.

[27] *MATLAB Version 9.12.0.1927505 (R2022a) Update 1*, The Mathworks, Natick, MA, USA, 2022.

[28] D. Silvera-Tawil, D. Rye, M. Soleimani, and M. Velonaki, "Electrical impedance tomography for artificial sensitive robotic skin: A review," *IEEE Sensors J.*, vol. 15, no. 4, pp. 2001–2016, Apr. 2015.

[29] A. Adler, A. Boyle, M. G. Crabb, B. L. Grychtol, W. R. B. Lionheart, H. F. J. Tregidgo, and R. Yerworth, "EIDORS version 3.9," in *Proc. 18th Int. Conf. Biomed. Appl.*, 2017, p. 63.

[30] S. Yong and K. Aw, "Modeling electrical resistance behavior of soft and flexible piezoresistive sensors based on carbon-black/silicone elastomer composites," *Sens. Imag.*, vol. 23, no. 1, p. 22, Dec. 2022.

[31] B. Esterer, J. Razenbock, M. Hollensteiner, D. Fuerst, and A. Schrempf, "Development of artificial tissue-like structures for a hybrid epidural anesthesia simulator," in *Proc. 38th Annu. Int. Conf. IEEE Eng. Med. Biol. Soc. (EMBC)*, Aug. 2016, pp. 2099–2102.

[32] B. Esterer, M. Hollensteiner, A. Schrempf, M. Winkler, S. Gabauer, D. Furst, R. Merwa, S. Panzer, K. Puschel, and P. Augat, "Characterization of tissue properties in epidural needle insertion on human specimen and synthetic materials," *J. Mech. Behav. Biomed. Mater.*, vol. 110, Oct. 2020, Art. no. 103946.

[33] M. Lee, C. Ang, K. Andreadis, J. Shin, and A. Rameau, "An open-source three-dimensionally printed laryngeal model for injection laryngoplasty training," *Laryngoscope*, vol. 131, no. 3, pp. 890–895, Mar. 2021.

[34] O. Alser, G. Youssef, S. Myers, and A. M. Ghanem, "A novel three-in-one silicone model for basic microsurgery training," *Eur. J. Plastic Surgery*, vol. 43, no. 5, pp. 621–626, Oct. 2020.

[35] J. M. Winter and C. Petropolis, "A novel silicone simulation model for microvascular anastomosis," *Plastic Surg.*, vol. 30, no. 2, pp. 113–116, May 2022.

[36] B. U. Gul, D. K. Yanilmaz, D. Arslan, M. Bayramicli, and O. Akbulut, "Silicone-based simulation models for peripheral nerve microsurgery," *J. Plastic, Reconstructive Aesthetic Surg.*, vol. 72, no. 3, pp. 477–483, Mar. 2019.

[37] H. Wi, H. Sohal, A. L. McEwan, E. Je Woo, and T. In Oh, "Multi-frequency electrical impedance tomography system with automatic self-calibration for long-term monitoring," *IEEE Trans. Biomed. Circuits Syst.*, vol. 8, no. 1, pp. 119–128, Feb. 2014.

[38] B. Buiantuev, N. Kalmykov, D. Kholodnyak, A. Brizic, L. Vincelj, and S. Hrabar, "Physically oriented design of negative capacitors based on Linvill's floating impedance converter," *IEEE Trans. Microw. Theory Techn.*, vol. 70, no. 1, pp. 139–154, Jan. 2022.

[39] F. Zamora-Arellano, O. R. López-Bonilla, E. E. García-Guerrero, J. E. Olguín-Tiznado, E. Inzunza-González, D. López-Mancilla, and E. Tlelo-Cuautle, "Development of a portable, reliable and low-cost electrical impedance tomography system using an embedded system," *Electronics*, vol. 10, no. 1, p. 15, Dec. 2020.

[40] S. Basan and E. Sancaktar, "Electrical conductivity of carbon black—Silicon rubber nanocomposites: Effects of strain, load and loading rate," *Current Nanomaterials*, vol. 1, no. 3, pp. 195–200, Jan. 2017.

[41] P. Wang and T. Ding, "Creep of electrical resistance under uniaxial pressures for carbon black–silicone rubber composite," *J. Mater. Sci.*, vol. 45, no. 13, pp. 3595–3601, Jul. 2010.

[42] H. Lee, D. Kwon, H. Cho, I. Park, and J. Kim, "Soft nanocomposite based multi-point, multi-directional strain mapping sensor using anisotropic electrical impedance tomography," *Sci. Rep.*, vol. 7, no. 1, pp. 1–10, Jan. 2017.

[43] S. Russo, R. Assaf, N. Carbonaro, and A. Tognetti, "Touch position detection in electrical tomography tactile sensors through quadratic classifier," *IEEE Sensors J.*, vol. 19, no. 2, pp. 474–483, Jan. 2019.

[44] J. Avery, D. Shulakova, M. Runciman, G. P. Mylonas, and A. Darzi, "Tactile sensor for minimally invasive surgery using electrical impedance tomography," *IEEE Trans. Med. Robot. Bionics*, vol. 2, no. 4, pp. 561–564, Nov. 2020.

[45] S. Russo, S. Nefti-Meziani, N. Carbonaro, and A. Tognetti, "Development of a high-speed current injection and voltage measurement system for electrical impedance tomography-based stretchable sensors," *Technologies*, vol. 5, no. 3, p. 48, Jul. 2017.

[46] Y. Zhang and C. Harrison, "Tomo: Wearable, low-cost electrical impedance tomography for hand gesture recognition," in *Proc. 28th Annu. ACM Symp. User Interface Softw. Technol.*, Nov. 2015, pp. 167–173.

[47] B. Pitaloka, A. Zarkasi, and D. R. Santoso, "Development of low cost EIT equipment for educational purposes," *J. Phys., Conf.*, vol. 1153, Feb. 2019, Art. no. 012041.

[48] H. Chen, X. Yang, P. Wang, J. Geng, G. Ma, and X. Wang, "A large-area flexible tactile sensor for multi-touch and force detection using electrical impedance tomography," *IEEE Sensors J.*, vol. 22, no. 7, pp. 7119–7129, Apr. 2022.

[49] K. Liu, Z. Qin, Y. Wu, B. Chen, F. Li, H. Pan, and J. Yao, "Fabrication of a tactile sensor for artificial skin based on electrical impedance tomography," *Biosensors Bioelectron., X*, vol. 10, May 2022, Art. no. 100116.

[50] H. Lee, H. Park, G. Serhat, H. Sun, and K. J. Kuchenbecker, "Calibrating a soft ERT-based tactile sensor with a multiphysics model and sim-to-real transfer learning," in *Proc. IEEE Int. Conf. Robot. Autom. (ICRA)*, May 2020, pp. 1632–1638.

[51] J. Zhu, C. Zhou, and M. Zhang, "Recent progress in flexible tactile sensor systems: From design to application," *Soft Sci.*, vol. 1, no. 1, p. 3, 2021.

[52] S. Yoshimoto, Y. Kuroda, and O. Oshiro, "Tomographic approach for universal tactile imaging with electromechanically coupled conductors," *IEEE Trans. Ind. Electron.*, vol. 67, no. 1, pp. 627–636, Jan. 2020.

[53] H. Park, K. Park, S. Mo, and J. Kim, "Deep neural network based electrical impedance tomographic sensing methodology for large-area robotic tactile sensing," *IEEE Trans. Robot.*, vol. 37, no. 5, pp. 1570–1583, Oct. 2021.

[54] C. Shao, S. Tanaka, T. Nakayama, Y. Hata, T. Bartley, Y. Nonomura, and M. Muroyama, "A tactile sensor network system using a multiple sensor platform with a dedicated CMOS-LSI for robot applications," *Sensors*, vol. 17, no. 9, p. 1974, Aug. 2017.

[55] T. Thurner. (2023). *Open Source Sensor Interface for Soft Detectors in Surgical Simulators*. [Online]. Available: https://github.com/tomtomHD/IMSC

THOMAS THURNER received the master's degree in mechatronics from Johannes Kepler University, in 2019, specializing in medical and biomechatronics. He is currently pursuing the joint Ph.D. degree with the Research Group of Martin Kaltenbrunner and the Research Group of Andreas Schrempf, focusing on the development of hybrid surgical simulators. His research interests include biosignal processing, medical technology, inkjet-printed electronics, and sensor technology, especially in soft structures.

ROLAND PRUCKNER received the master's degree in physics from Johannes Kepler University, in 2019. He is currently pursuing the joint Ph.D. degree with the LIT Soft Materials Laboratory and the Research Group of Martin Kaltenbrunner, Soft Matter Physics Division. He is specialized in soft and sustainable electronics.

MARTIN KALTENBRUNNER (Member, IEEE) received the master's and Ph.D. degrees in physics from Johannes Kepler University, Linz, under the supervision of Siegfried Bauer, in 2008 and 2012, respectively, and the Habilitation (Venia Docendi) in experimental physics in "soft electronics," in 2016. He joined the Someya-Sekitani Laboratory for Organic Electronics, The University of Tokyo, as a Postdoctoral Researcher, leading the "Imperceptible Electronics Team." Returning to JKU, in 2014, as an Assistant Professor. In 2019, he was appointed as a Full Professor with Johannes Kepler University. He is currently a Full Professor with Johannes Kepler University, heading the Soft Matter Physics Division and the LIT Soft Materials Laboratory. His research group specializes in soft electronics and soft transducers, in particular on sustainable and biodegradable elastic materials and processes for skin-inspired electronics and embodied robotics. They are pioneers in soft and stretchable batteries and solar cells and ultrathin and lightweight electronic foils. The group develops materials strategies, design rules and technologies including resilient yet degradable soft and elastic substrates, passive and active components and power sources that enable green wearable (bio)electronics, and soft robots.
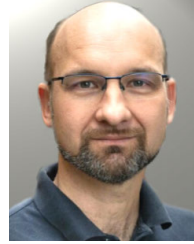
ANDREAS SCHREMPF received the master's and Ph.D. degrees with Johannes Kepler University, Linz, in 1998 and 2004, respectively. He is currently a Professor in biomechanics and computer modeling and simulation with the Department of Medical Engineering, Upper Austria University of Applied Sciences. After working as a Senior Researcher with the Linz Competence Center in Mechatronics, he moved to the University of Applied Sciences, Upper Austria, in 2005. His research interests include modeling and simulation in biomechanics and biomedical engineering and their application to the development of hybrid surgical simulators.

• • •